Damage evolution characteristics of 3D reconstructed bedding-containing shale based on CT technology and digital image processing

Zhonghu Wu[1] · Yuhan Yang[1] · Yujun Zuo[2] · Xiangrui Meng[1] · Wentao Wang[3] · Wenli Lei[1]

Abstract

In order to construct a numerical simulation model that can reflect the bedding structure of real shale samples, CT scanning and digital image processing were utilized to analyze the intricate internal structure of the shale. By integrating this information with RFPA3D finite element software, a 3D non-uniform numerical model that can accurately represent the shale bedding structure was built and simulated for direct tensile tests. The experimental findings demonstrated that shale possesses noticeable anisotropic properties with regard to tensile strength. Two distinct modes of damage were observed in shale specimens subjected to uniaxial tensile loading: tensile damage along the bedding plane and damage occurring perpendicular to the bedding plane. The spatial distribution characteristics of the acoustic emission points better reflect the damage pattern of the specimen, and the acoustic emission counting evolution characteristics are closely related to the damage process of the specimen. These research findings shed light on the fracture damage mechanism of shale formations, thereby contributing to a better understanding of the engineering stability evaluation for rock bodies. Furthermore, they offer a novel perspective for investigating the evolution of damage in rock particles.

Keywords Shale · CT scanning technology · Digital image processing · Numerical simulation · Fracture processes

Introduction

Shale gas is an unconventional clean energy source. In recent years, it has become a new research hotspot in the energy industry (Lei et al. 2021; Bilgen and Sarıkaya 2016; Meakin et al. 2013; Wang and Li 2017). Shale gas resources in China are widely distributed, with the advantages of large resource reserves, a high energy conversion rate, and a low pollution index. It provides a good development platform for energy acquisition and also shows a good development prospect for energy utilization and promotion (Zou et al. 2010; Hao

et al. 2013; Ma et al. 2018). At present, the main method of extracting shale gas is hydraulic fracturing. There are still many engineering challenges and a lack of technology for shale gas mining, both domestically and abroad. The study of the physical properties and fracture patterns of shales is an important reference for the improvement of hydraulic fracturing techniques. Typically, subterranean sedimentary rocks exhibit geological discontinuities, including intriguing features like bedding planes. Distinguished by their distinctive material composition, color, and structural arrangement in comparison with the shale matrix, these bedding planes play a crucial role. Notably, the orientation of these planes significantly influences the anisotropic characteristics of shale, encompassing its mechanical properties and deformation characteristics. Consequently, this intricate relationship gives rise to a more complex destruction mechanism, signifying a substantial impact on shale gas extraction. (Heng et al. 2015, 2020; Ma et al. 2020). The study of the dip effect of shale laminae is not only to ensure the stability of the rock during the extraction of shale gas, but also to provide a strong guarantee for the study of the propagation path of hydraulic fractures and the stability analysis of shale

✉ Zhonghu Wu
wuzhonghugzu@163.com

1 College of Civil Engineering, Guizhou University, Guiyang 550025, China

2 Mining College, Guizhou University, Guiyang 550025, China

3 School of Mechanics and Civil Engineering, China University of Mining and Technology, Beijing 100083, China

wells, which is of great significance for the efficient and safe extraction of shale gas.

At present, many scholars, domestically and abroad, have achieved many results on the anisotropy of bedding shale. Xu et al. conducted uniaxial compression tests on specimens perpendicular and parallel to the bedding to investigate the effects of bedding planes on shale wave velocity and acoustic emission (AE) properties (Xu et al. 2017). Gao et al. measured the compressive and tensile strengths of the shale and also studied the properties of the shale by nondestructive wave velocity measurements. The shale exhibited strongly anisotropic behavior, with tensile strengths perpendicular to the bedding plane much greater than those parallel to the bedding plane. The results of ultrasonic tests show that both compressional and shear wave velocities show strongly anisotropic patterns (Gao et al. 2015). Luo et al. conducted a three-point bending test on shale to study its anisotropic fracture extension behavior, and the results showed that the fracture tip stress field in anisotropic shale is not only determined by the stress intensity factor, but also related to the elastic constant and bedding plane tilt angle (Luo et al. 2018). Lei et al. observed the microfracture process of shale by scanning electron microscopy and simulated the effects of different bedding properties on the fracture behavior of shale using a finite element model. The results showed that the mechanical properties of weak laminar planes had significant effects on fracture mode, tensile strength, fracture toughness, crack initiation angle, crack extension path, and complex fracture network generation (Lei et al. 2021). Guo et al. conducted static and dynamic compressive tests on dry and water-saturated shale specimens with bedding dips of 0°, 30°, 45°, 60°, and 90°. The results show that the compressive parameters are most affected by waterlogging when the lamina plane dips at 45° or 60° (Guo et al. 2021). Most of the above studies are experimental and theoretical studies on shale under compressive stress, while most of the studies on shale under tensile stress are by indirect tensile methods, such as the Brazilian splitting test. However, Hudson et al. (1972) pointed out that the largest equivalent force in the Brazilian splitting test did not occur at the center of the specimen but at the end face of the loading point. The damage is usually caused by the stress concentration at the loading point of the pad, which is inconsistent with the empirical formula of the Brazilian splitting test. It has been found through theoretical research that there is an obvious three-dimensional effect in the Brazilian splitting test, and the thickness of the Brazilian disk greatly affects its strength (Chau and Wei 2001; Lavrov and Vervoort 2002). Fairhurst (1964) pointed out that the results measured by the Brazilian splitting test were lower than the actual values. Therefore, the tensile strength obtained by the splitting test is not as accurate as the direct tensile test.

There are few research results about the direct stretching action. There are two main reasons for this: First, due to the limitations of test conditions, general mechanical testing machines and testing devices cannot determine the deformation and damage laws of rocks under the action of tensile stress. Secondly, for the direct tensile test of the rock specimen, processing both ends of the fixed is more difficult. Therefore, the problem of connecting the specimen to the testing machine has also been investigated (Nova and Zaninetti 1990). However, the non-uniformity of the specimens and the lack of precision in the fabrication of the specimens in laboratory tests can also lead to large errors. The limitations of indoor physical tests have made numerical simulation an increasingly powerful tool for studying rock damage. At present, numerical simulation is widely used in geotechnics, petroleum, and shale gas extraction. Numerical simulation can fully consider the non-uniform characteristics of rocks and complex force conditions, and it has the incomparable advantages of laboratory physical tests and field tests. He et al. used PFC2D finite element software to simulate the Brazilian splitting test and established a numerical model of rocks containing double fractures to analyze the indirect tensile mechanical behavior of anisotropic disk specimens (He et al. 2021). Zhang et al. used RFPA-dynamic to build a numerical model to investigate the impact performance and mechanism of different numbers of prefabricated parallel cracks on specimens (Zhang et al. 2020). The above studies are all based on the two-dimensional case to consider the damage to rocks, while the real rock mechanics problems occur in three-dimensional space. Regarding the numerical simulation of the damage to the 3D problem, different 3D models have been constructed. Wu et al. (2022) created a three-dimensional equivalent discrete fracture network model based on RFPA3D finite element software that can effectively analyze the effect of water head on the hydraulic properties of fractured rock masses. Some scholars have established a three-dimensional numerical model using finite element software and simulated the straight shear test, SHPB test, and Brazilian splitting test to investigate the rupture mechanism of the specimens (Dai et al. 2015; Liao et al. 2020; Zhang et al. 2021). CT scanning technology is a nondestructive testing means; CT images can truly reflect the internal pores and mineral structure of the rock. In recent years, many scholars have applied CT scanning technology to research in the field of unconventional oil and gas and have made some research progress (Dong et al. 2018; Li et al. 2017; Zhou et al. 2016; Duan et al. 2022). The integration of CT scanning techniques into numerical simulations is also a relatively new research methodology. The parameters of most value models are qualitative statistical parameters, and such numerical models constructed from statistical distributions do not reflect the true fine structure of the rock.

Based on the above research, this paper uses CT scanning technology to obtain images of shale internal slices, reconstructs 3D numerical models based on realistic fine structure CT images by RFPA3D software, and conducts tensile tests to study the damage pattern, tensile strength, and acoustic emission properties of shales with different laminar dip angles. The 3D model constructed by this method is identical to the fine structure of the pores and minerals of the real rock sample, making the numerical model closer to the physical model. This study provides an effective method to study the influence of the fine structure of rocks on their mechanical behavior, provides theoretical and methodological support for the determination of the tensile strength parameters of rocks, and has certain theoretical significance and engineering application value for rock mechanics testing methods and engineering applications.

Specimen and CT scanning technology

The instrument used in this CT scan experiment is an X-ray 3D ultra-precision micro-nanostructure detector (Fig. 1). The instrument model is nanoVoxel-3502E, the X-ray source voltage of the instrument is 20–190 kV, and the highest spatial resolution of the instrument can reach 0.5 µm. The CT scanning system can identify fractures and pores at the micron scale. A large field-of-view flat detector and an objective-coupled detector are used together for test imaging, with an optical magnification system to reduce the size of the detector unit and improve resolution.

The specimens used in this experiment are from the Lower Cambrian Niutitang Formation in the northern part of Guizhou Province. Samples were taken by core drilling to a diameter of 50 mm and a height of 100 mm (Fig. 2a). The lithology of the study area is predominantly black carbonaceous shale, with the shale matrix appearing gray and the laminated surfaces appearing gray-black.
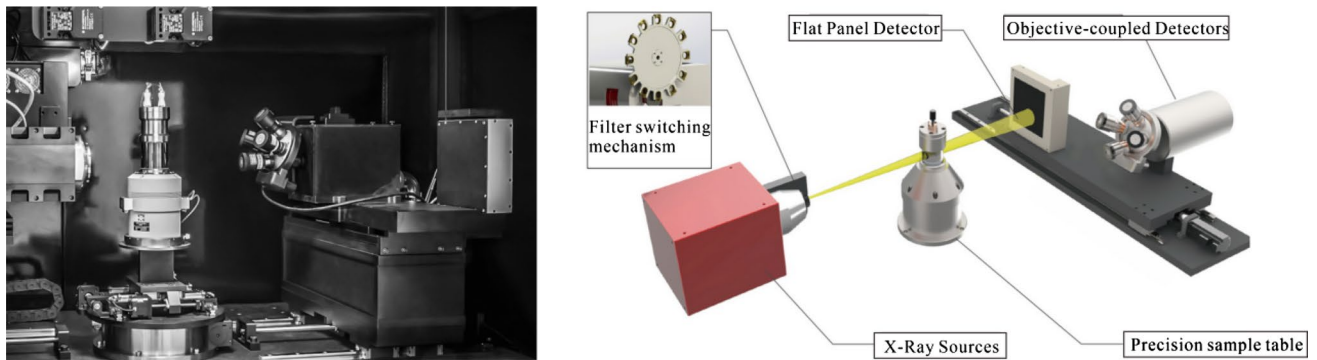

Fig. 1 X-ray 3D microscopic imaging system

(a) Shale specimen　　(b) CT scanning image in XZ plane　　(c) CT scanning image in XY plane
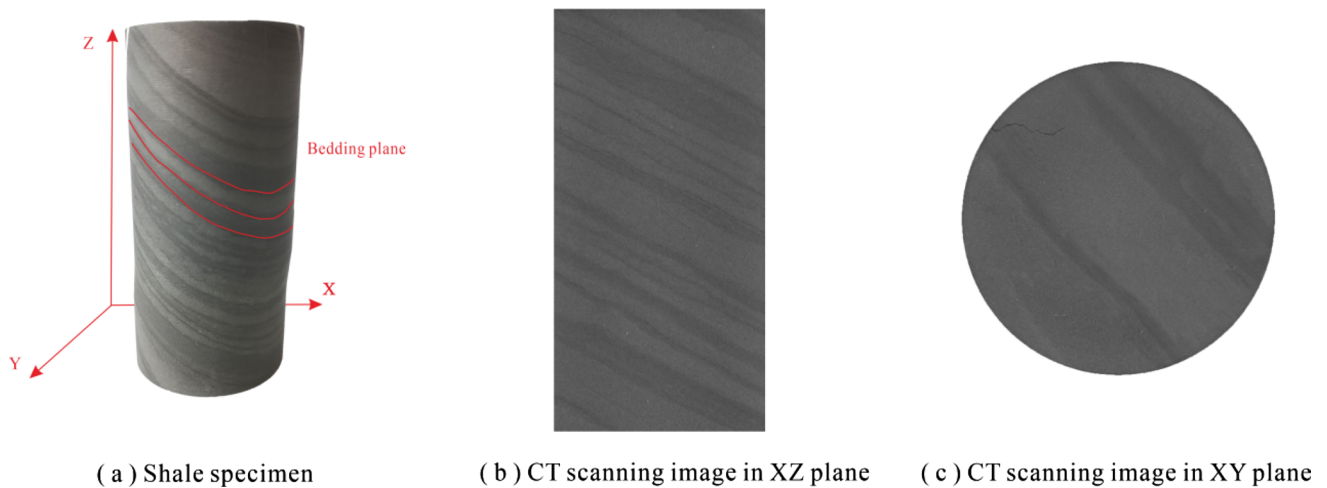
Fig. 2 Specimen and CT scanning images

We placed the shale specimens on the specimen table for CT scanning and obtained CT scans in three planar directions (Fig. 2b, c). 5480 images were scanned in the XY plane, and 2740 images were scanned in the XZ and YZ planes, with a slice image of 1814×1246 pixels and a scan interval of approximately 18.22 μm per layer.

CT image preprocessing

As the gray-scale values of the bedding and the shale matrix are relatively close in the CT scan images, threshold segmentation cannot clearly distinguish the bedding from the shale matrix. Therefore, it is necessary to preprocess CT images, of which the spatial domain processing technology is the most basic processing; the basic principle is to process the pixel points of the image itself; the principle of mathematical expression is as follows:

$$g(x, y) = T[f(x, y)],\qquad(1)$$

where $f(x,y)$ is the input known original image; $g(x,y)$ is the processed result; and T is the operator defined on a field of points (x,y) to process the original image f.

In this study, CT images are binarized to obtain microstructural information in the images by binarization. The binarization principle is as follows: A threshold I in the HSI color space (0–255) is selected. The I value represents the intensity of the color, the higher the I value, the brighter the color. If a pixel in the image has a gray value greater than or equal to the threshold I, its gray value is redefined as 255 (white); if a pixel has a gray value less than the threshold I, its gray value is redefined as 50 (gray-black). The difference

in gray-scale values between the rock matrix and the bedding in CT scan images is used to characterize the internal microstructure of the shale specimen, and the bedding and shale matrix are separated by binarization.

To determine the binarization image segmentation threshold, a scan line AA' is selected that passes through both the shale matrix and the bedding using the method of Yang et al. (2023), and the gray-scale value of each pixel point on this scan line is counted. As shown in Fig. 3, the gray-scale values of the bedding in the scanned image are below the dashed line, and the gray-scale values of the shale matrix are above the dashed line. The CT images were binarized according to the following equation (Lang et al. 2019; Yuan et al. 2023):

$$g(x, y) = \begin{cases} 255 & f(x, y) \geq I \\ 50 & f(x, y) < I, \end{cases}\qquad(2)$$

where $f(x, y)$ is the initial gray value of pixel point (x, y) and $g(x, y)$ is the gray value of pixel point (x, y) after the binarization process.

In this study, the histogram threshold method and the comparison method were employed to determine the threshold value I. Initially, statistical analysis was performed using digital image analysis software to explore the relationship between gray-scale values and the corresponding pixel counts in the CT image (Fig. 4). The analysis revealed that the main pixel points were concentrated within the I range of 73–108. Since there is a need to segment two different substances within this I range, four thresholds ($I = 78$, $I = 88$, $I = 98$, and $I = 108$) were initially set for comparison. Figure 5a–d depicts the binarized CT images obtained using these different thresholds. It is observed that different
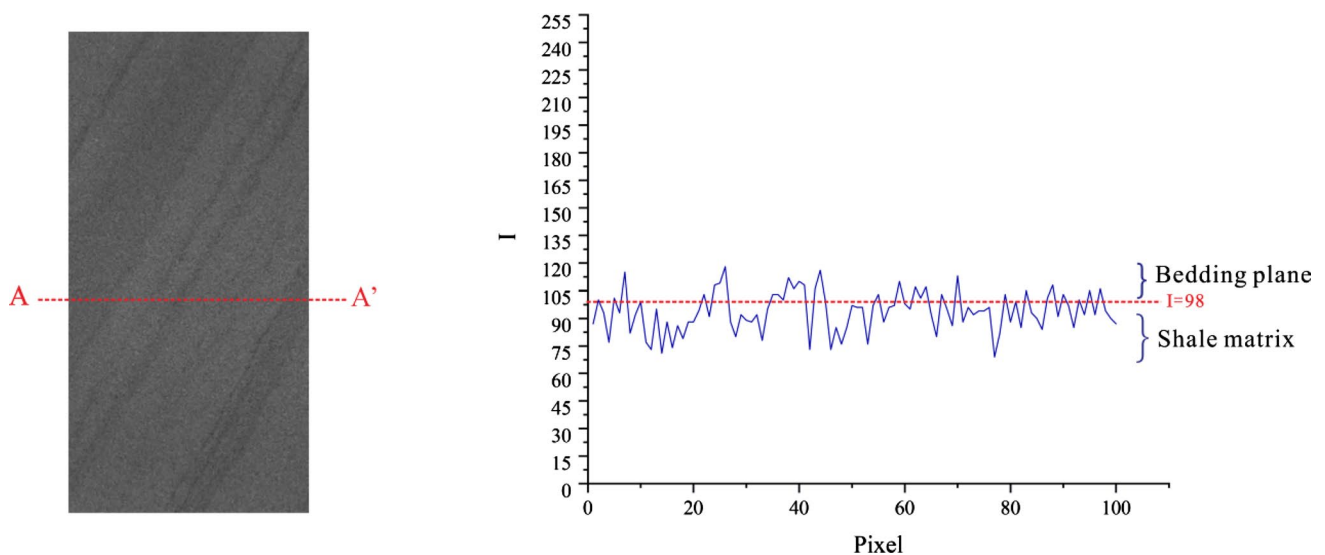

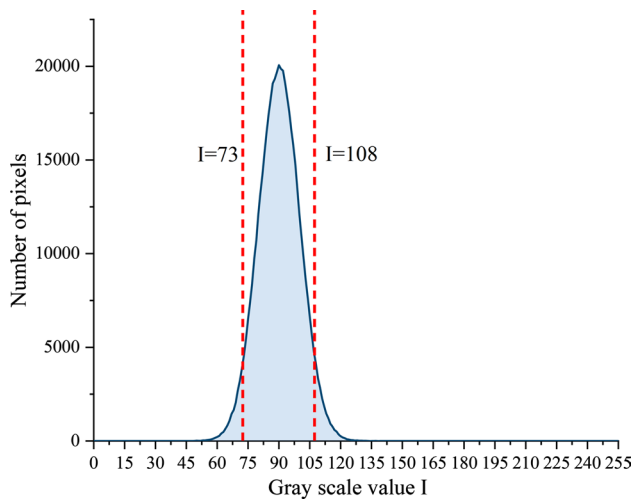**Fig. 3** Gray value along scanned line

Fig. 4 Gray-scale histogram

matrix as bedding planes. After conducting multiple threshold segmentation comparison tests, an *I* value of 98 was ultimately selected for threshold segmentation in this study.

Figure 6 shows the CT image processing process. From the binarization-processed image, it is found that there are still many noise points in the processed image, which will have an impact on the identification of the bedding plane when constructing the numerical model and may also affect the experimental results of the numerical simulation. Therefore, it is necessary to perform denoising processing. We employed in-house numerical image processing software to perform noise reduction on binarized CT images. Figure 6c shows the image after the denoising processing, at which the structural information of the shale matrix and bedding plane can be clearly identified.

Three-dimensional model reconstruction

The modeling principle of RFPA3D finite element software is as follows: converting a picture into vectorized data means treating each pixel point as a finite element mesh. The images are superimposed in the order of the CT scans, and it is assumed in the reconstruction process that the slice images can represent the fine structure of a material with a very small thickness d. If d is small, the error in the fine structure characterization can be neglected.

To build cylindrical 3D digital specimens of shale with different bedding inclinations, 100 CT images of XZ sections
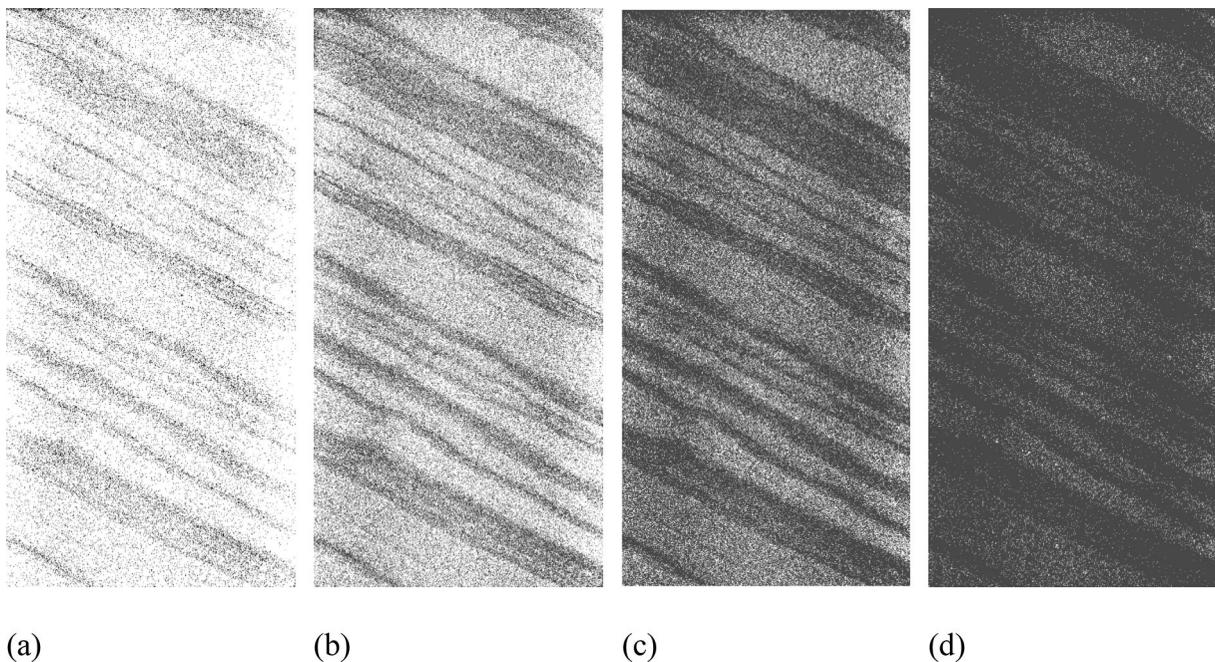
I values yield varying segmentation effects. For instance, Fig. 5a with a relatively low threshold results in the loss of numerous pixel points representing the bedding plane. Although Fig. 5b represents an improvement, there still remains a discontinuity in the bedding plane, with several pixel points mistakenly recognized as shale matrix. Comparatively, Fig. 5c exhibits a clearer and more continuous representation of the bedding plane, but with a slightly low threshold. Meanwhile, Fig. 5d depicts a high threshold, leading to the misclassification of several parts of the shale

(a)   (b)   (c)   (d)

Fig. 5 Effect of binarization under different I value segmentation, **a** *I* = 78, **b** *I* = 88, **c** *I* = 98, **d** *I* = 108

were uniformly selected for superimposition. Due to the limited computing power, the pixels of CT images were reduced to 200×100. Hundred digital images of the representative shale fine structure were imported into RFPA3D for superimposition, and the constructed 3D model contains a total of 2 million elements, each with a size of $0.5\ mm \times 0.5\ mm$. By rotating and cropping the CT images to achieve different angles of laminar inclination, Fig. 7 shows the schematic diagram of the model building process. The final 3D numerical model size is a standard cylindrical specimen with a diameter of 50 mm and a height of 100 mm.

To adequately capture the fine-scale non-uniformity present in rock material properties, RFPA makes an assumption regarding the mechanical properties of discretized fine-scale primitives. It is posited that these properties obey a specific statistical distribution law, namely the Weibull distribution (Williams 1957). This assumption serves to precisely account for the distinctive, discrete characteristics exhibited by rock-like media. The assignment of values for strength, Poisson's ratio, modulus of elasticity, and density of the fine-scale unit follows the equation presented below (Zuo et al. 2022):

$$f(x) = \frac{m}{\beta} \cdot \left(\frac{x}{\beta}\right)^{m-1} \cdot e^{-\left(\frac{x}{\beta}\right)^{m}}, x \geq 0, \tag{3}$$

where x denotes the parameters of the physical properties of the base element of the material medium (elastic modulus, strength, Poisson's ratio, density, etc.); β denotes the average value of the physical properties of the base element; m indicates the nature parameter of the distribution function, whose physical meaning reflects the homogeneity of the material medium, defined as the homogeneity coefficient of the material medium, reflecting the degree of homogeneity of the material; and $f(x)$ is the statistical distribution density of the physical properties x of the material (rock) primitive. The material parameters used in this numerical experiment are based on the study of shales of the Lower Cambrian Niutitang Formation in the northern part of Guizhou Province by Wu et al. (2020). Each parameter is summarized in Table 1, and the value in parentheses indicates the value of m used for that parameter.

Following the importation of CT images into RFPA3D, the software promptly discerns the unique gray values present within the images. Pixels characterized by a gray value of 255
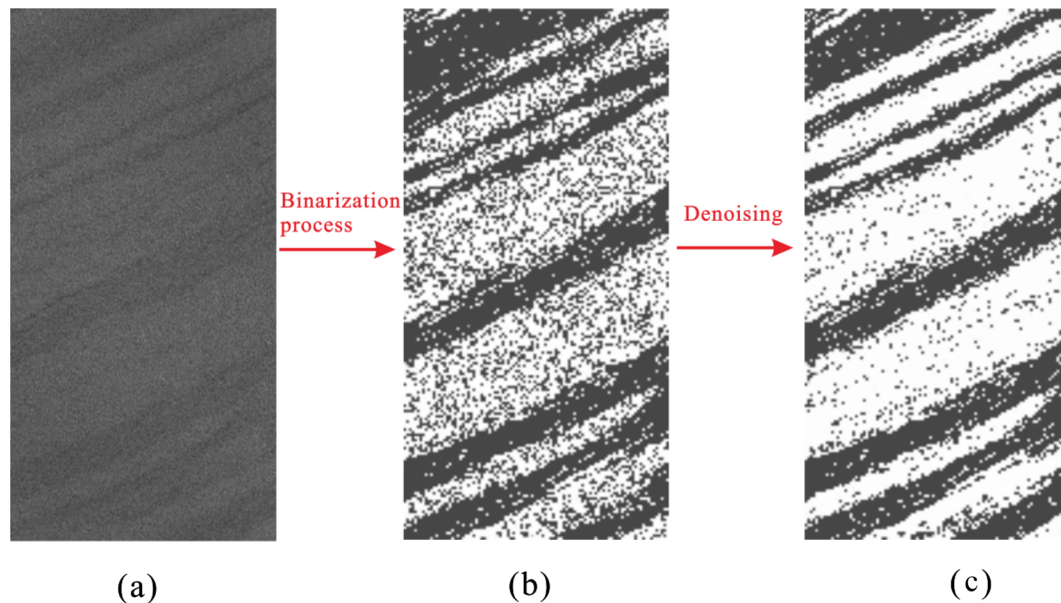

(a)   (b)   (c)

Fig. 6 CT image binarization and denoising processing

Table 1 Shale specimen material parameter table

Materials	Modulus of elasticity (GPa)	Poisson's ratio	Compressive strength (MPa)	Friction angle (°)	Pull-to-pressure ratio
Shale matrix	51.6 (5)	0.22 (200)	145.63 (5)	35	14
Bedding	30.96 (2)	0.31 (200)	116.00 (2)	30	13

are designated as representing the shale matrix, while pixels displaying a gray value of 50 are identified as indicative of the bedding plane. Subsequently, each fundamental parameter and non-uniformity coefficient pertaining to both the shale matrix and bedding plane are inputted. Figure 7 shows the numerical modeling of shale with five groups of different bedding plane inclinations. In Fig. 7, the formation of five distinct sets of shale numerical models is depicted. These models exhibit varying inclinations of the bedding plane, namely 0°, 30°, 45°, 60°, and 90°, while one additional group of models serves as a control set with no presence of a bedding plane. In total, six groups of models are generated for analysis. The standard specimen utilized in these models possesses a diameter of 50 mm and a height of 100 mm. The loading direction is set to the Z-axis, and the displacement loading method is adopted, with the initial displacement of −0.0001 mm/step, and the loading displacement of −0.0002 mm/step at each step until the specimens are damaged.

The principle of RFPA3D

A simple intrinsic model of elastic damage, the tensile Mohr–Coulomb damage criterion, is used in RFPA3D (Liang et al. 2012). As soon as the minimum principal stress of the element reaches the uniaxial tensile strength, the element will undergo tensile damage. Mohr–Coulomb criterion with tensile damage criterion is shown in Eq. (4):

$$
\begin{cases}
\sigma_1 - \dfrac{1 + \sin\varphi}{1 - \sin\varphi}\sigma_3 \geq \sigma_c & \sigma_1 > \sigma_c - \lambda\sigma_t \\
\sigma_3 \leq -\sigma_t & \sigma_1 \leq \sigma_c - \lambda\sigma_t,
\end{cases}
\tag{4}
$$

where $\lambda = \frac{1+\sin\varphi}{1-\sin\varphi} = \tan^2\theta$, $\theta = \frac{\pi}{4} + \frac{\varphi}{2}$, which is the shear breaking angle.
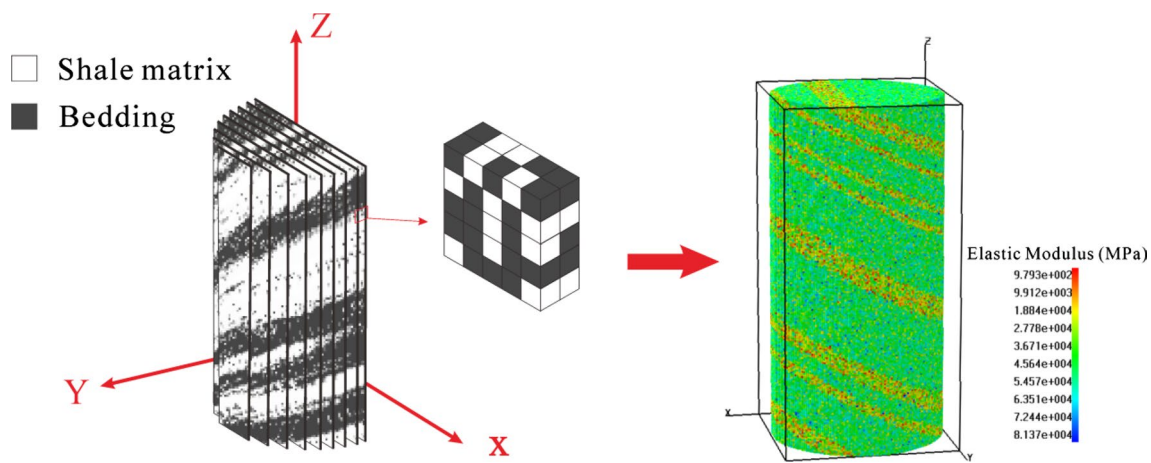
The tensile damage evolution can be expressed as follows:

$$
D =
\begin{cases}
0 & (\varepsilon < \varepsilon_{t0}) \\
1 - \dfrac{\sigma_{rt}}{\varepsilon E_0} & (\varepsilon_{t0} \leq \varepsilon \leq \varepsilon_{ut}) \\
1 & (\varepsilon > \varepsilon_{ut}),
\end{cases}
\tag{5}
$$

where σ_{rt} is the residual strength of the element, ε_{t0} is the minimum principal strain threshold at which tensile damage occurs, and ε_{tu} is the minimum principal strain threshold at which element separation occurs. Tensile damage is described by the intrinsic structure relationship shown in Fig. 8.

$$
\bar{\varepsilon} = \sqrt{\langle\varepsilon_1\rangle^2 + \langle\varepsilon_2\rangle^2 + \langle\varepsilon_3\rangle^2},
\tag{6}
$$

where $\langle\varepsilon_i\rangle$ is functions defined as follows:

$$
\langle\varepsilon_i\rangle =
\begin{cases}
\varepsilon_i & (\varepsilon_i \leq 0, i = 1, 2, 3) \\
0 & (\varepsilon_i > 0, i = 1, 2, 3).
\end{cases}
$$

Numerical simulation results and analysis

Uniaxial tensile test results analysis

Figure 9 shows the stress–strain curves for each bedding dip specimen. It can be seen from Fig. 9 that the axial peak intensity of the specimen gradually increases with the increase in the bedding dip angle. The peak axial tensile strength is the smallest when the inclination angle is 0°, and the peak tensile strength is the largest when the inclination angle is 90°. This indicates that the peak strength of the shale exhibits significant anisotropy as the dip angle of the laminae increases. The specimens at different angles exhibit obvious elastic-brittle characteristics.

Figure 10 shows the trend of tensile strength and anisotropy coefficient of the bedding plane of shale at different azimuth
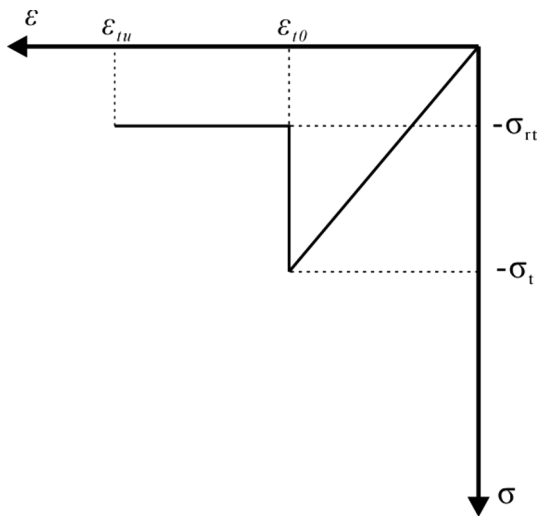

Fig. 7 Schematic diagram of the modeling process based on CT images

Fig. 8 Damage constitutive law for an element in tensile failure mode
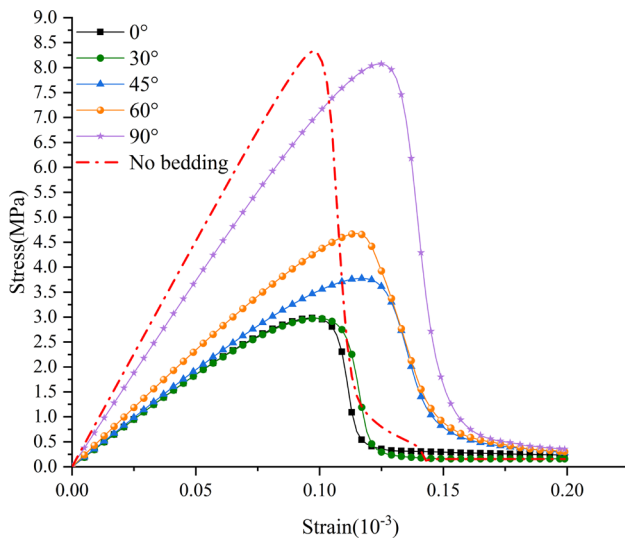

Fig. 9 Stress–strain curve

angles, and the specimens at different angles are smaller than the tensile strength of no bedding specimens. It indicates that the spatial distribution pattern of brittle minerals within the shale matrix has a significant effect on the tensile strength. To characterize the effect of structural effects of bedding on the tensile strength anisotropy of shale, the tensile strength of the no bedding specimen is taken as the reference value, the tensile strength of the remaining angles is taken as the variable, the anisotropy coefficient $S(\theta)$ is the dependent variable, and the functional relationship equation is as follows:

$$S(\theta) = 1 - \frac{\sigma(\theta)}{\sigma^m}, \tag{7}$$

where σ^m is the uniaxial tensile strength of the no bedding specimen; $\sigma(\theta)$ is the uniaxial tensile strength at any angle.

The tensile properties of shale with laminations have been measured by many scholars. Table 1 compiles the tensile strength measurements of shale with bedding plane at angles of 0°, 45°, and 60° in a number of studies, and it can be seen that all of the studies satisfy the law that the tensile strength of the specimens increases as the angle of bedding inclination increases. However, most of the tests were performed by indirect stretching (Brazilian split test), and only a few studies measured the tensile strength of shale by means of direct stretching, and even fewer studies investigated the tensile properties of shale under direct stretching by means of numerical simulations. As can be seen from the figure, the numerical simulation results of the present study are in excellent agreement with the results of the laboratory tests by Jin et al. (Jin et al. 2018), indicating the validity of the present modeling approach (Fig. 11).

Damage pattern analysis

Figure 12 shows the internal element damage maps at the end of loading for specimens with different bedding inclination angles, and the dark blue color in the figure represents the already damaged elements. As can be seen from the figure, the damage units of the specimens at 0°–45° are basically concentrated on the bedding, and almost no tensile damage occurs on the shale matrix. At bedding dip angles of 45° and 60°, cracks appear not only on the bedding plane, but also on the shale matrix where damage occurs (marked locations). As the dip angle increases, it can be seen that the main fracture does not only extend along the bedding, but also extends laterally on the shale matrix. The 90° specimen has breakage elements scattered throughout the interior, producing a more complex crack geometry. Indicating the existence of a threshold angle $\theta*$, when the lamina dip angle $\theta < \theta*$, the damage mode is mainly manifested as tensile damage along the bedding plane; when the laminar dip angle $\theta > \theta*$, it exhibits a composite tensile damage pattern along the bedding plane and the shale matrix. Hobbs (Barron 1971) proposed a damage criterion for the variation of bedding rock specimens with the dip angle of the bedding according to Griffith fracture theory, where the critical bedding dip angle $\theta*$ can be determined by the following equation:

$$\cos\theta * (1 + \cos\theta *) = \frac{2T_0}{T_{90}}, \tag{8}$$

where θ is the inclination angle of the bedding; T_0 is the tensile strength of the specimen with 0° inclination angle of the bedding; and T_{90} is the tensile strength of the specimen

Fig. 10 Trends of tensile strength, elastic modulus, and lateral and bedding effect coefficients of shale under different Azimuth angles
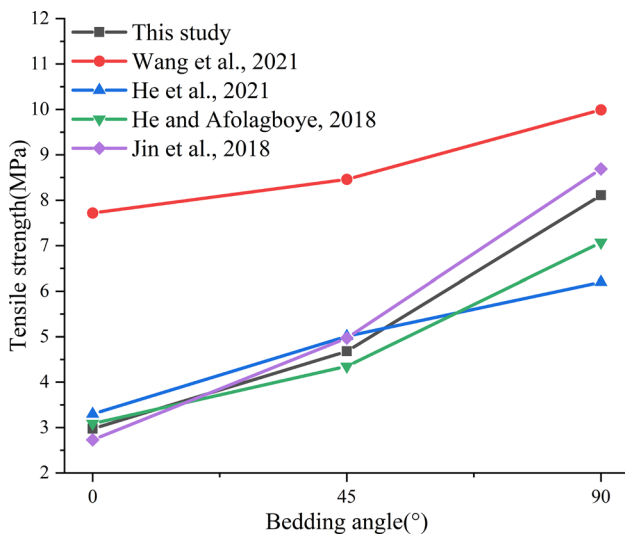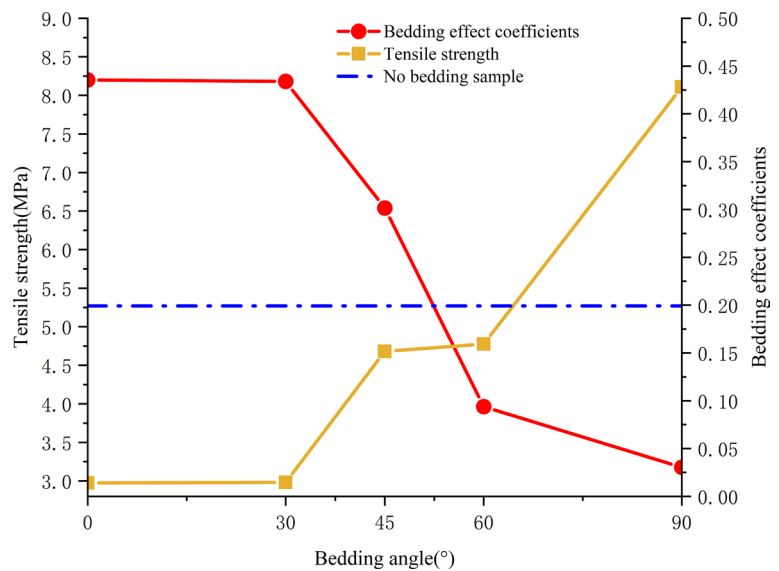

Fig. 11 Comparison of this study with other studies

with 90° inclination angle of the bedding. Substituting the data into the above equation yields $\theta^* = 46.44°$.

Figure 13 shows the direct tensile damage mode of the bedding shale specimen, and the direct tensile of the bedding shale exhibits two main damage modes. It is assumed that T_b is the bedding tensile strength value, and T_m is the matrix tensile strength value. When the dip angle of the bedding is 0°, the damage pattern of the rock sample is shown in Fig. 13a. The damage plane, in this case, is the bedding plane, so it can be considered that the tensile strength of the rock sample is equal to that of the bedding plane, which can be expressed as $\sigma_t = \sigma_1 = T^b$. When $0° < \theta < \theta^*$, the damage pattern is shown in Fig. 13b. For the stress at the midpoint of the specimen with bedding inclination, the stress can be

decomposed along and perpendicular to the bedding direction to obtain Eq. 7:

$$\begin{cases} \sigma_y = \sigma_1 \cos^2 \theta \\ \sigma_x = \sigma_1 \sin \theta \cos \theta. \end{cases} \tag{9}$$

If the bedding plane is to produce tensile damage, the magnitude of the positive stress should be equal to the magnitude of the tensile strength of the bedding material, i.e., $\sigma_y = T^b$ and the magnitude of the tensile strength of the rock mass can be obtained as $\sigma_t = \sigma_1 = T^b / \cos^2 \theta$. This can explain the gradual increase in the tensile strength of the rock specimens as the dip angle of the bedding increases. With the gradual increase in the dip angle of the bedding, when $\theta > \theta^*$, it shows a step-like damage pattern (Fig. 13c, d). Suppose the destruction area of the shale matrix is A_i. In order for the destruction of the shale matrix to occur, it should be $\sigma_i = T^m$, and we can get $F_i = T^m A_i$; therefore, $F = \sum F_i = T^m \sum A_i$, $\sigma_t = \frac{T^m \sum A_i}{A}$. Due to the presence of bedding plane, it is obvious that $\sum A_i < A$, i.e., $\sigma_t < T^m$. Therefore, the mechanism of increasing the tensile strength of bedding rock specimens with the increase in laminae can be explained and analyzed from the perspective of elastic mechanics.

Analysis of the damage process

Since the rupture process and rupture mode of 0°–45° specimens are basically the same, this paper only analyzes the detailed damage process for 0°, 60°, and 90° specimens. A total of four different stages of z-axis loading displacement maps were selected for the crack initiation, extension,
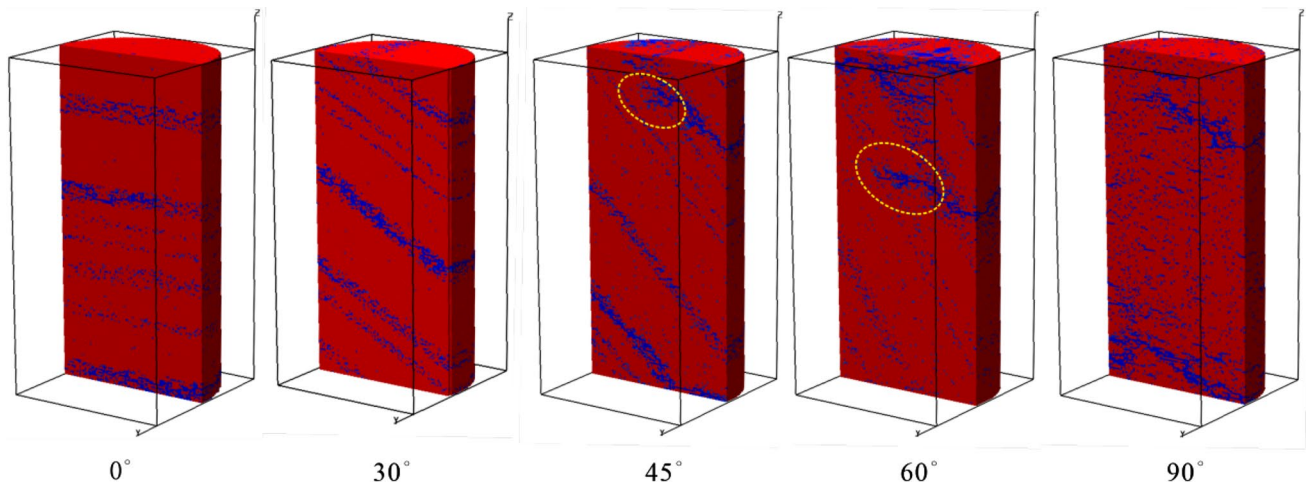
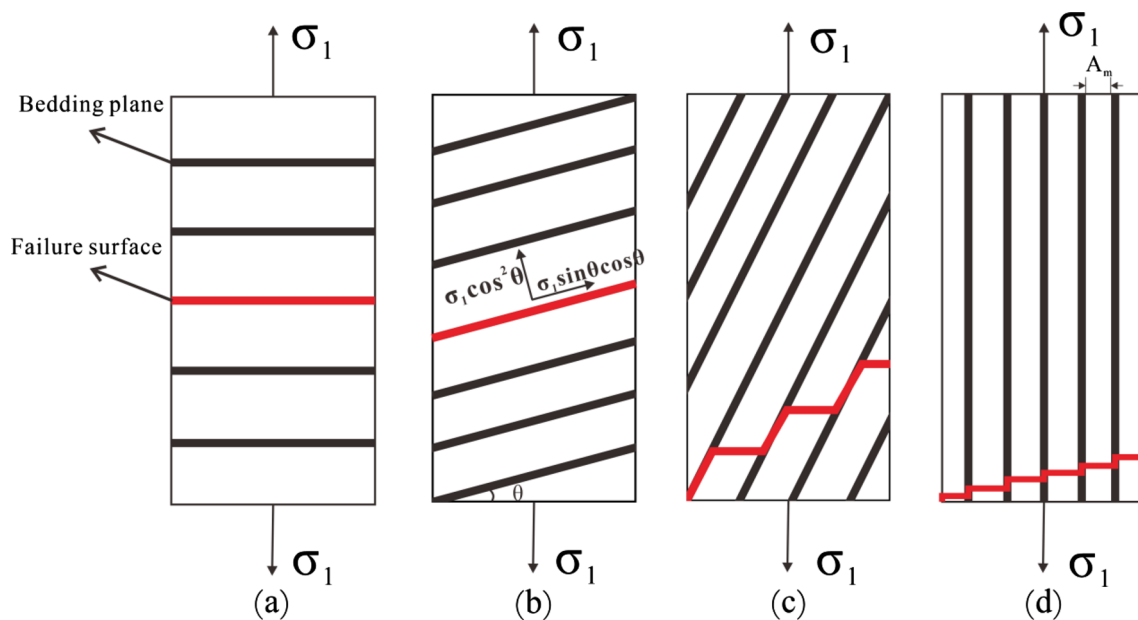**Fig. 12** Elemental damage images of shale models during late loading period

Fig. 13 Tensile failure mechanism analysis of the layered rocks

penetration, and damage stages, respectively. In order to clearly reveal the rupture process, the internal destruction process is also shown. Figure 14 shows the progressive damage process of the 0° specimen, from which it can be seen that initially some rupture units are produced in the laminar surface at the top, middle, and bottom of the specimen.

Figure 14 shows the progressive damage process of the 0° specimen, from which it can be seen that initially some rupture units are produced in the bedding plane at the top, middle, and bottom of the specimen. As the load increases, the initial crack gradually extends from the loading end along the bedding plane and forms a surface crack, and eventually,

the crack penetrates the entire specimen and the specimen is pulled off. Comparing the elastic modulus diagrams, it can be seen that the whole process produced only primary cracks on the bedding plane, with fewer secondary cracks, and three tensile fracture planes on the bedding plane at the top, middle, and bottom of the specimen. This property is usually attributed to the bedding structure of the shale. Figure 15 shows the progressive damage process of the 60° specimen, which is similar to that of the 0° specimen in the early stage of loading, where cracks first appear on the bedding but are not completely penetrated. As the loading proceeds, cracks begin to develop at the end of the specimen
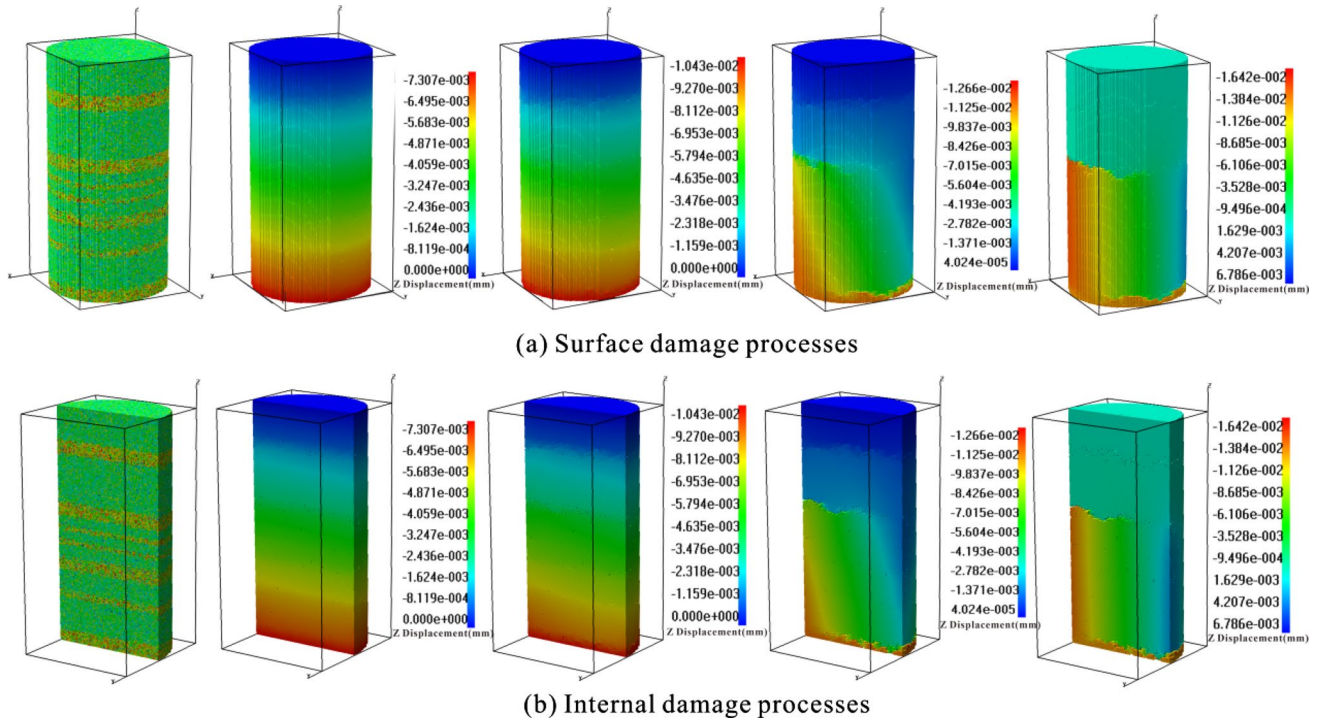
(a) Surface damage processes

(b) Internal damage processes

Fig. 14 Failure process of specimen 0°: displacement in *z* direction

(a) Surface damage processes
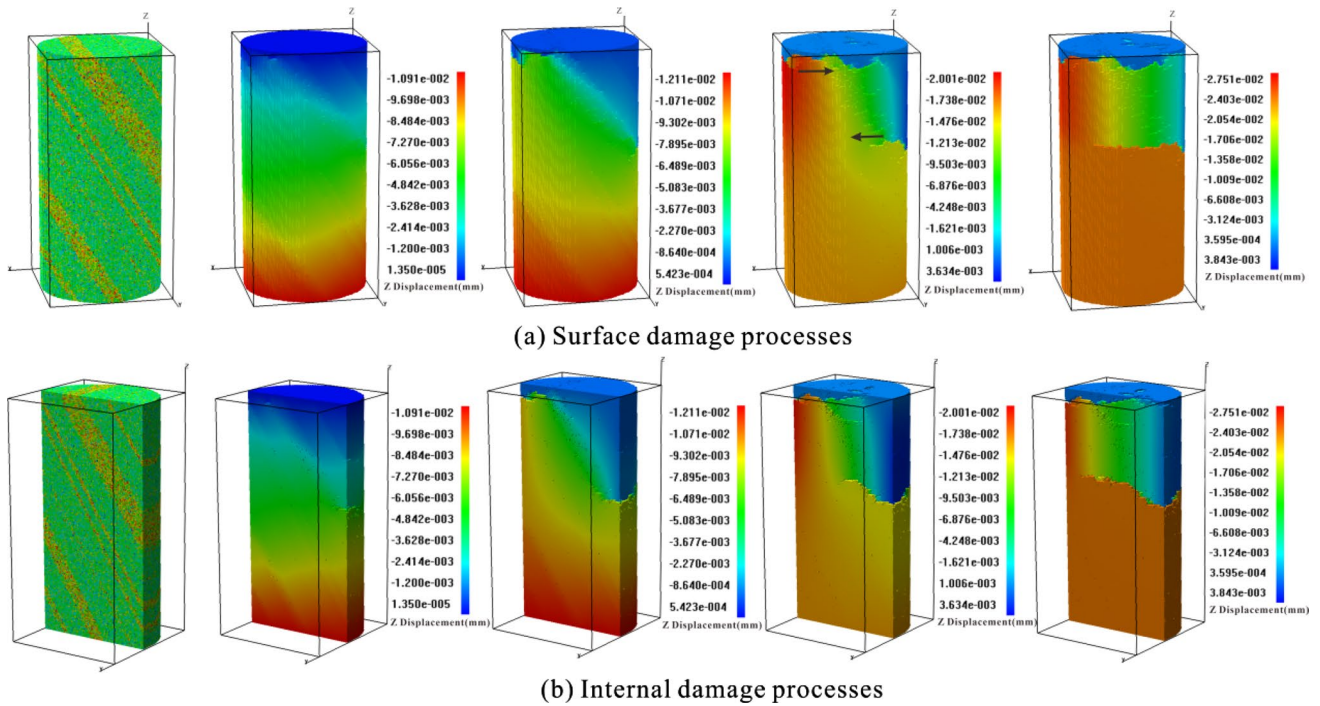

(b) Internal damage processes

Fig. 15 Failure process of specimen 60°: displacement in *z* direction

and extend laterally in the shale matrix (marked locations), creating two main cracks in the upper and middle parts of the specimen, eventually forming two tensile fracture planes almost perpendicular to the loading direction. Figure 16
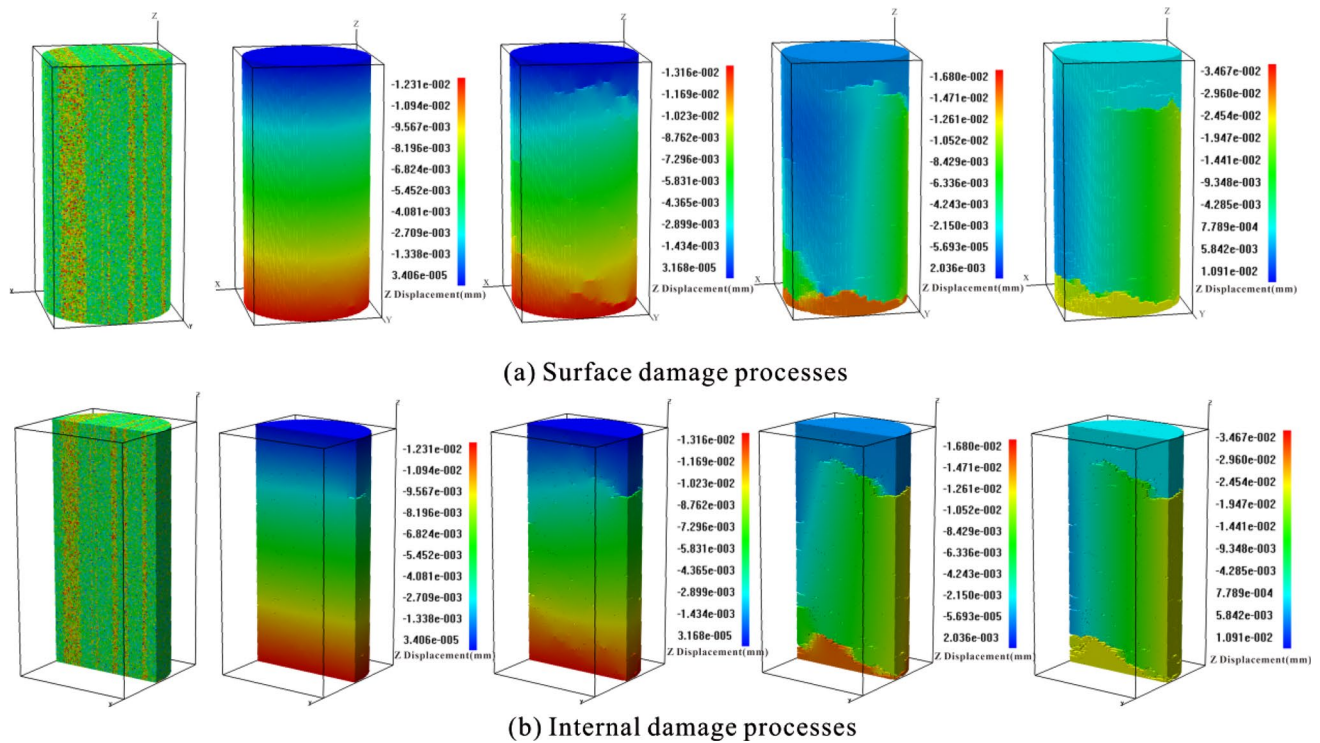
(a) Surface damage processes

(b) Internal damage processes

Fig. 16 Failure process of specimen 90°: displacement in *z* direction

shows the progressive damage process of the 90° specimen. In the early stage of loading, many microcracks will be generated inside the specimen. As the loading proceeds, the bedding plane expands laterally at an approximately vertical angle, producing tensile fracture surfaces at the top and bottom of the specimen, and eventually, the specimen fractures due to the expansion of the two main cracks. In contrast to the damage process in the 60° specimen, the cracks in the 90° specimen did not follow the extension of the bedding plane but instead underwent tensile damage directly on the shale matrix.

From the above analysis, it can be concluded that the dip angle of the lamina surface has a greater influence on the direction of crack extension. The cracks in the 0°–45° specimens basically extend along the bedding plane; the cracks in the 60° specimens first develop and extend on the bedding plane, and then the main crack develops on the bedding at the edge of the specimen and extends approximately transversely to the other end; the 90° specimen first produces a few microcracks throughout the specimen, followed by a main crack from the edge and lateral expansion, which eventually penetrates the specimen.

Acoustic emission characterization

When the internal structural units of a brittle material are damaged, acoustic energy is released, and this rapid release of energy in a localized area can be referred to as acoustic emission (AE). The acoustic emission characteristics are related to the whole loading process, and the pattern of acoustic emission can reflect the damage degree of the structure. Figure 17 shows the spatial distribution of acoustic emission points for each specimen over three different periods.

The spatial evolution of acoustic emission shows that at the beginning of loading, a small number of acoustic emission points appear on the bedding plane of each group of specimens, and with the increase in stress level, the acoustic emission points gradually increase. In the middle of loading, there is a large amount of element destruction on the bedding plane, and the acoustic emission points increase dramatically at this time. When the peak stress is reached, the bedding plane of the specimen at 0°–60° is covered by a large number of acoustic emission points. When reaching the end of loading, acoustic emission occurs only on a few main cracks, and the damage plane can be clearly seen at this stage. Some acoustic emission points appear irregularly at the beginning of the loading of the 90° specimen, and in the middle of the loading, the whole specimen is covered with a
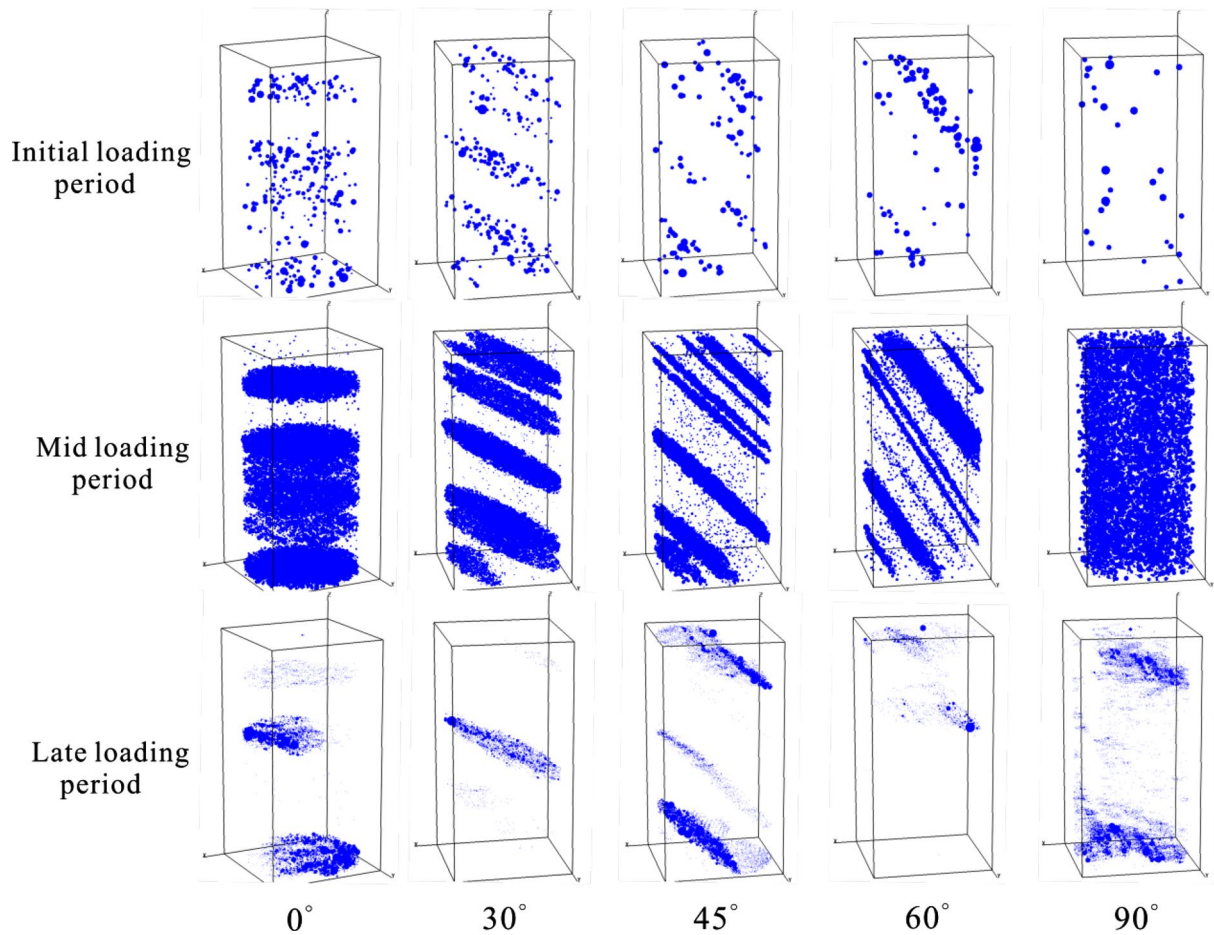
Fig. 17 Spatial distribution of acoustic emission points at different dip angles and stress levels

large number of densely packed acoustic emission points. At the end of loading, the acoustic emission points are distributed near the loading end, indicating that the damage plane appears at this location.

Since the failure of a specimen element releases the elastic energy stored during deformation, it is assumed that the failure of each element represents the source of an acoustic event. By recording the number of damaged cells at each step and the cumulative number of damaged cells, RFPA3D is able to obtain a graph of the evolution of the number of acoustic emissions over time during the loading of the specimen.

Figure 18 illustrates the trends of stress, AE, and cumulative AE with strain for five groups of different bedding dip angles. From the figure, it can be seen that the whole acoustic emission process shows a single-peak distribution pattern, i.e., only one peak in the acoustic emission count occurs during the whole loading process. It indicates that the damage

to the specimen is a transient process, and the brittle damage to the bedding shale is clearly characterized. From the count of acoustic emissions, the larger the inclination of the bedding plane, the higher the number of acoustic emissions. The cumulative number of acoustic emissions at the destruction of the 90° specimen was up to more than 210,000, and the cumulative number of acoustic emissions at the 0° specimen was just over 120,000. This is due to the difference in damage mode. From the damage mode analysis above, it is known that the specimens below the threshold angle $\theta*$ are basically only damaged on the bedding plane, and only the elements on the bedding plane undergo acoustic emission. The rupture plane is flatter, and the area of the rupture plane is smaller, so the number of acoustic emissions is lower. And the composite damage to the laminar and matrix planes occurs for specimens above the threshold angle. The fracture plane shows a stepped shape, and the damage area is also larger, so the number of acoustic emissions is higher.
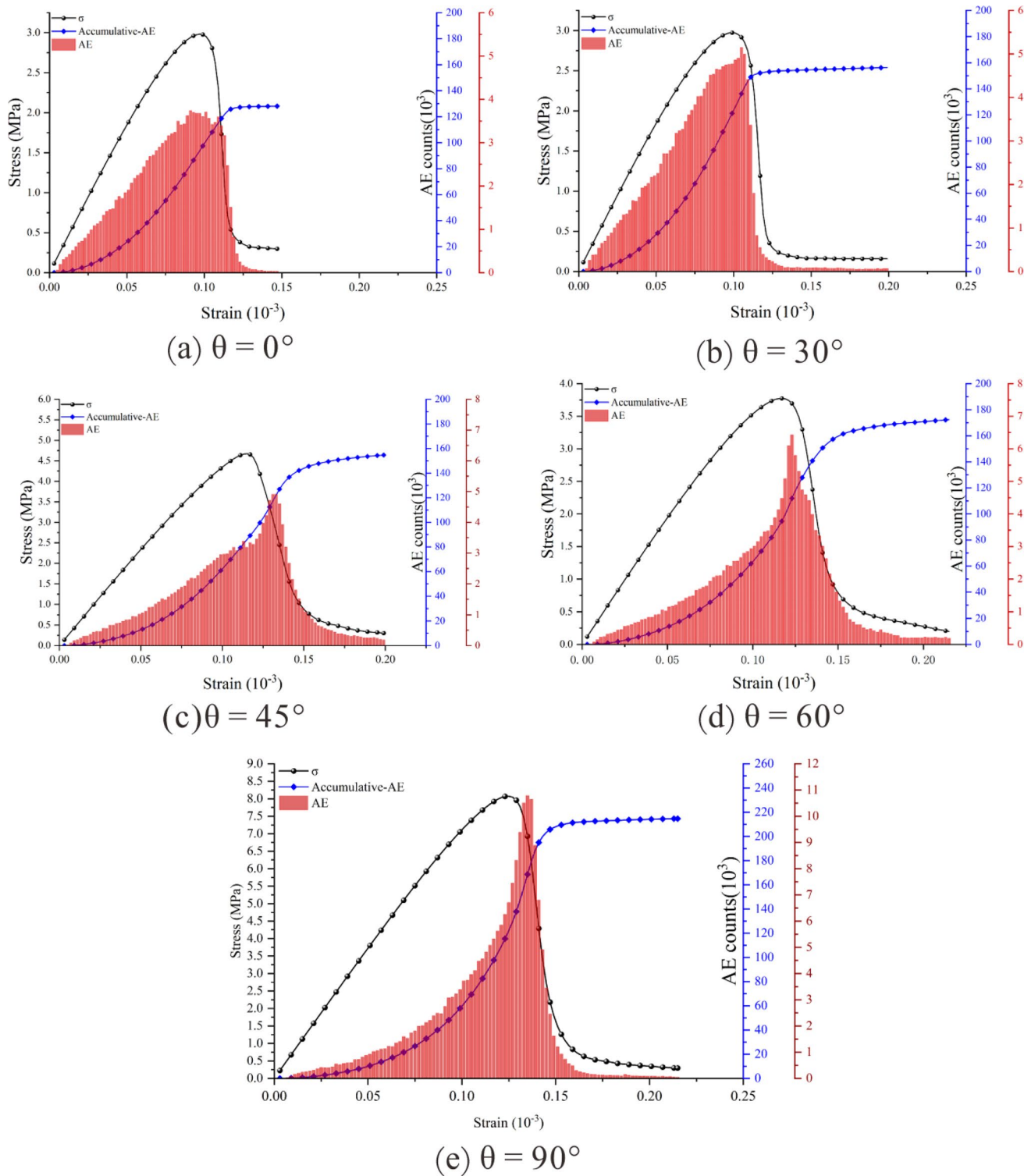
Fig. 18 Trends of stress, AE count and cumulative AE count with strain at different angles

In summary, the spatial distribution characteristics of the acoustic emission points better reflect the macroscopic damage pattern of the specimens, which is consistent with the analysis results of the above damage pattern. There is a certain correlation between the acoustic emission characteristics and the fracture mode of the specimen, and this correlation is mainly manifested as follows: With the increase in the lamina dip angle, the acoustic emission count increases, and the larger

the angle, the more obvious the single-peak distribution of the acoustic emission count curve.

Discussion

The approach elucidated in this study offers a partial resolution to the intricate challenges encountered in 3D reconstruction, binarization processing, and threshold segmentation within the realm of digital rock technology. The derived numerical simulation outcomes not only aid in comprehending the fracture damage mechanisms inherent to rock formations, but also lay a solid foundation for the evaluation of rock engineering stability. Despite promising preliminary findings, it is important to acknowledge the existence of certain limitations within this study. Continued research endeavors are necessary to further explore the establishment of numerical modeling techniques as well as the comprehensive understanding of petrophysical properties associated with shale gas reservoirs.

Primarily, the model implemented in this paper adequately captures the fundamental structural characteristics of shale bedding. However, it falls short of encompassing the intricate microfeatures and structural intricacies inherent in shale formations. This simplification is a result of certain factors, including the limitations imposed by CT scanning. Notably, if the size of the bedding plane or pores within the shale is smaller than the scanning recognition unit, they cannot be adequately visualized in the CT scanning images. Additionally, the recognition capabilities of the imaging system are constrained by CT noise, making it challenging to accurately identify and depict exceedingly small bedding planes or pores during the noise removal process. Lastly, computational limitations restrict the smallest scale at which the constructed model can effectively characterize bedding planes or pores. To address these limitations, it is recommended that future investigations explore the utilization of high-computing-power computers in conjunction with high-resolution CT images. This combination would facilitate the construction of more refined and realistic 3D models, enabling multiscale modeling to discern the impacts of nanoscale components.

Secondly, it is imperative to acknowledge the significant challenges posed by conducting direct tensile physical experiments on natural rock specimens. The outcomes of physical direct tensile tests are influenced by end effects, a factor that was not considered in the boundary conditions of the numerical simulations employed in this study. To enhance the replication of real physical tests, it is recommended that forthcoming research endeavors incorporate direct tensile numerical simulation tests that account for the presence of end effects. Moreover, the

uncontrollable nature of natural sample preparation further compounds the complexities associated with this line of inquiry. Ensuring a consistent set of rocks and bedding planes with identical geometric parameters seems implausible, making it difficult to replicate tests under different boundary conditions. As previously mentioned in the introduction, the challenges inherent in physical experiments served as one of the driving forces behind the authors' pursuit of investigating the mechanisms underlying the tensile strength of bedding plane shale through numerical methods.

Conclusion

In this study, a comprehensive analysis of shale damage evolution was conducted through the construction of a three-dimensional model of the actual fine structure, utilizing slice images acquired via CT scanning technology and integrating them with RFPA3D software. The investigation encompassed the examination of various aspects, including the stress–strain curve, stress evolution at characteristic intensity points, crack extension and deformation patterns, as well as the fracture process. Through meticulous analysis, the inquiry yielded the following conclusive findings:

1. Reconstructing the three-dimensional model based on CT images and computationally simulating the damage evolution process can observe the expansion and penetration process of cracks on the surface and inside the shale specimen, solving the difficult problem of observing the internal damage of rocks and providing a feasible method for the in-depth study of the mechanical mechanism of rocks.

2. The anisotropic nature of the strength of the shale specimens was obvious, with the tensile strength reaching a minimum value of 2.97 MPa at $\theta = 0°$ and a maximum value of 5.07 MPa at $\theta = 90°$. When the dip angle of bedding is small, the tensile strength of bedding shale is less influenced by the dip angle of bedding, and the direct tensile strength of bedding rock mainly depends on the mechanical properties of bedding; when the dip angle of bedding is large, the direct tensile strength of bedding rock mainly depends on the mechanical properties of rock materials. The reason for this result is mainly that the bedding plane belongs to the weak plane in the shale structure with a weak degree of cementation, which is more likely to form fractures under the action of a tectonic stress field or during hydraulic fracturing.

3. The shale specimens exhibit two damage modes under the action of tension. There exists a critical dip angle $\theta*$; when the dip angle of the bedding angle $\theta < \theta*$, it exhib-

its the damage mode of tension along the bedding plane, and when the dip angle of the bedding angle $\theta > \theta^*$, it exhibits the compound tensile damage mode along the bedding plane and the shale matrix.

4. The spatial distribution characteristics of the acoustic emission points are directly related to the damage pattern of the shale specimens, and the spatial distribution characteristics of the acoustic emission points better reflect the macroscopic damage pattern of the specimens. The locations of microfractures inside the shale samples and the development trend of fractures during the whole damage evolution are qualitatively described. The acoustic emission count curve is mainly characterized by a single-peak distribution. When the specimen is tensioned along the bedding plane, the growth of the acoustic emission curve is gentler, and when the specimen is tensioned along the bedding and shale matrix, the acoustic emission count shows a steep increase.

Declarations

Conflict of interest The authors declare that they have no known competing financial interests or personal relationships that could have appeared to influence the work reported in this paper.

References

Barron K (1971) Brittle fracture initiation in and ultimate failure of rocks: part I—anisotropic rocks: theory. In: International journal of rock mechanics and mining sciences and geomechanics abstracts. Elsevier, pp 553–563. https://doi.org/10.1016/0148-9062(71)90026-X

Bilgen S, Sarıkaya İ (2016) New horizon in energy: shale gas. J Nat Gas Sci Eng 35:637–645. https://doi.org/10.1016/j.jngse.2016.09.014

Chau K, Wei X (2001) A new analytic solution for the diametral point load strength test on finite solid circular cylinders. Int J Solids Struct 38(9):1459–1481. https://doi.org/10.1016/S0020-7683(00)00122-0

Dai F, Wei M, Xu N, Ma Y, Yang D (2015) Numerical assessment of the progressive rock fracture mechanism of cracked chevron notched Brazilian disc specimens. Rock Mech Rock Eng 48(2):463–479. https://doi.org/10.1007/s00603-014-0587-8

Dong H et al (2018) 3D pore-type digital rock modeling of natural gas hydrate for permafrost and numerical simulation of electrical properties. J Geophys Eng 15(1):275–285. https://doi.org/10.1088/1742-2140/aa8a8e

Duan Y, Feng X, Li X, Yang B (2022) Mesoscopic damage mechanism and a constitutive model of shale using in-situ X-ray CT device. Eng Fract Mech. https://doi.org/10.1016/j.engfracmech.2022.108576

Fairhurst C (1964) On the validity of the 'Brazilian'test for brittle materials. In: International journal of rock mechanics and mining

sciences and geomechanics abstracts. Elsevier, pp 535–546. https://doi.org/10.1016/0148-9062(64)90060-9

Gao Q, Tao J, Hu J, Yu X (2015) Laboratory study on the mechanical behaviors of an anisotropic shale rock. J Rock Mech Geotech Eng 7(2):213–219. https://doi.org/10.1016/j.jrmge.2015.03.003

Guo Y, Li X, Huang L, Liu H, Wu Y (2021) Effect of water-based working fluid imbibition on static and dynamic compressive properties of anisotropic shale. J Nat Gas Sci Eng 95:104194. https://doi.org/10.1016/j.jngse.2021.104194

Hao F, Zou H, Lu Y (2013) Mechanisms of shale gas storage: Implications for shale gas exploration in China. AAPG Bull 97(8):1325–1346. https://doi.org/10.1306/02141312091

He B, Liu J, Zhao P, Wang J (2021) PFC2D-based investigation on the mechanical behavior of anisotropic shale under Brazilian splitting containing two parallel cracks. Front Earth Sci 15(4):803–816. https://doi.org/10.1007/s11707-021-0895-8

Heng S, Guo Y, Yang C, Daemen J, Li Z (2015) Experimental and theoretical study of the anisotropic properties of shale. Int J Rock Mech Min Sci 74:58–68. https://doi.org/10.1016/j.ijrmms.2015.01.003

Heng S, Li X, Liu X, Chen Y (2020) Experimental study on the mechanical properties of bedding planes in shale—ScienceDirect. J Nat Gas Sci Eng. https://doi.org/10.1016/j.jngse.2020.103161

Hudson J, Brown ET, Rummel F (1972) The controlled failure of rock discs and rings loaded in diametral compression. In: International journal of rock mechanics and mining sciences and geomechanics abstracts. Elsevier, pp 241–248. https://doi.org/10.1016/0148-9062(72)90025-3

Jin Z, Li W, Jin C, Hambleton J, Cusatis G (2018) Anisotropic elastic, strength, and fracture properties of Marcellus shale. Int J Rock Mech Min Sci 109:124–137. https://doi.org/10.1016/j.ijrmms.2018.06.009

Lang Y, Liang Z, Duan D, Cao Z (2019) Three-dimensional parallel numerical simulation of porous rocks based on CT technology and digital image processing. Rock Soil Mech 40(3):1204–1212. https://doi.org/10.16285/j.rsm.2017.1728. (**in Chinese with English Abstract**)

Lavrov A, Vervoort A (2002) Theoretical treatment of tangential loading effects on the Brazilian test stress distribution. Int J Rock Mech Min Sci 39(2):275–283. https://doi.org/10.1016/S1365-1609(02)00010-2

Lei B et al (2021) Experimental and numerical investigation on shale fracture behavior with different bedding properties. Eng Fract Mech 247:107639. https://doi.org/10.1016/S1365-1609(02)00010-2

Li J et al (2017) Pore-scale investigation of microscopic remaining oil variation characteristics in water-wet sandstone using CT scanning. J Nat Gas Sci Eng 48:36–45. https://doi.org/10.1016/j.jngse.2017.04.003

Liang Z, Xing H, Wang S, Williams DJ, Tang C (2012) A three-dimensional numerical investigation of the fracture of rock specimens containing a pre-existing surface flaw. Comput Geotech 45(SEP.):19–33. https://doi.org/10.1016/j.compgeo.2012.04.011

Liao Z, Ren M, Tang C, Zhu J (2020) A three-dimensional damage-based contact element model for simulating the interfacial behaviors of rocks and its validation and applications. Geomech Geophys Geo-Energy Geo-Resour 6(3):1–21. https://doi.org/10.1007/s40948-020-00171-z

Luo Y et al (2018) Linear elastic fracture mechanics characterization of an anisotropic shale. Sci Rep 8(1):1–12. https://doi.org/10.1038/s41598-018-26846-y

Ma Y, Cai X, Zhao P (2018) China's shale gas exploration and development: understanding and practice. Pet Explor Dev 45(4):589–603. https://doi.org/10.1016/S1876-3804(18)30065-X

Ma X, Xie J, Yong R, Zhu Y (2020) Geological characteristics and high production control factors of shale gas reservoirs in Silurian

Longmaxi Formation, southern Sichuan Basin. SW China Pet Explor Dev 47(5):901–915. https://doi.org/10.1016/S1876-3804(20)60105-7

Meakin P, Huang H, Malthe-Sørenssen A, Thøgersen K (2013) Shale gas: opportunities and challenges. Environ Geosci 20(4):151–164. https://doi.org/10.1306/eg.05311313005

Nova R, Zaninetti A (1990) An investigation into the tensile behaviour of a schistose rock. Int J Rock Mech Min Sci Geomech Abstracts 27(4):231–242. https://doi.org/10.1016/0148-9062(90)90526-8

Wang Q, Li R (2017) Research status of shale gas: a review. Renew Sustain Energy Rev 74:715–720. https://doi.org/10.1016/j.rser.2017.03.007

Williams ML (1957) On the stress distribution at the base of a stationary crack. https://doi.org/10.1115/1.4011454

Wu Z et al (2020) Acoustic and fractal analyses of the mechanical properties and fracture modes of bedding-containing shale under different seepage pressures. Energy Sci Eng 8(10):3638–3656. https://doi.org/10.1002/ese3.772

Wu N, Liang Z, Zhang Z, Li S, Lang Y (2022) Development and verification of three-dimensional equivalent discrete fracture network modelling based on the finite element method. Eng Geol 306:106759. https://doi.org/10.1016/j.enggeo.2022.106759

Xu F et al (2017) Effect of bedding planes on wave velocity and AE characteristics of the Longmaxi shale in China. Arab J Geosci 10(6):1–10. https://doi.org/10.1007/s12517-017-2943-y

Yang Y, Wu Z, Zuo Y, Song H, Wang W, Tang M, Cui H (2023) Three-dimensional numerical simulation study of pre-cracked shale based on CT technology. Front Earth Sci 10:1120630. https://doi.org/10.3389/feart.2022.1120630

Yuan C, Nie W, Li Q, Geng J, Dai B, Gao J (2023) Automatic batch recognition of rock deformation areas based on image segmentation methods. Front Earth Sci 10:1093764. https://doi.org/10.3389/feart.2022.1093764

Zhang Y et al (2020) Impact failure of flattened Brazilian disc with cracks—process and mechanism. J Wuhan Univ Technol Mater Sci Ed 35(5):1003–1010. https://doi.org/10.1007/s11595-020-2348-8

Zhang Y et al (2021) Experimental and numerical study on the dynamic fracture of flattened Brazilian discs with prefabricated cracks. Eng Fract Mech 254:107885. https://doi.org/10.1016/j.engfracmech.2021.107885

Zhou G, Zhang Q, Bai R, Ni G (2016) Characterization of coal micropore structure and simulation on the seepage rules of low-pressure water based on CT scanning data. Minerals 6(3):78. https://doi.org/10.3390/min6030078

Zou C et al (2010) Geological characteristics and resource potential of shale gas in China. Pet Explor Dev 37(6):641–653. https://doi.org/10.1016/S1876-3804(11)60001-3

Zuo Y, Hao Z, Liu H, Pan C, Lin J, Zhu Z et al (2022) Mesoscopic damage evolution characteristics of sandstone with original defects based on micro-ct image and fractal theory. Arab J Geosci 15(22):1673. https://doi.org/10.1007/s12517-022-10896-8